JOURNAL OF CATALYSIS 142, 206–225 (1993)

Carbon Monoxide Hydrogenation on Cobalt Foil and on Thin Cobalt Film Model Catalysts

J. LAHTINEN,[1] T. ANRAKU,[2] AND G. A. SOMORJAI[3]

Materials Science Division, Lawrence Berkeley Laboratory and Department of Chemistry, University of California, Berkeley, California 94720

Received August 31, 1992; revised March 12, 1993

Carbon monoxide hydrogenation has been studied on polycrystalline cobalt foils and on thin cobalt films evaporated on gold substrate, using a combination of UHV studies and atmospheric pressure reactions, in the temperature range from 475 to 575 K and at 101 kPa total pressure. On the cobalt foils we have detected C_1–C_4 hydrocarbons and on the Co/Au surfaces C_1–C_3 hydrocarbons. The activation energy of methane formation is the same for both types of surfaces (~86 kJ/mol), but the CO and H_2 partial pressure dependencies of the rate are different. For Co/Au surfaces the reaction rate increases with increasing partial pressures of both H_2 and CO, but on cobalt foils the CO pressure dependence is negative, as for the supported cobalt catalysts reported in the literature. On cobalt foil the CO hydrogenation reaction proceeds via CO dissociation, followed by subsequent hydrogenation of surface carbon, whereas in the Co/Au system the rate-limiting step is either formation or dissociation of a CHOH-complex. Auger electron spectroscopy shows no excessive carbon build-up during the reaction on any of the cobalt surfaces below 550 K.

1. INTRODUCTION

The use of cobalt in catalyzing the hydrogenation of carbon monoxide to produce liquid hydrocarbons (Fischer–Tropsch synthesis) goes back to 1920s (*1*, *2*). In spite of the impressive catalytic properties and promising chemisorption properties for other surface science applications, cobalt has not been widely studied by the various techniques of modern surface science as compared to its neighbors on the periodic table (iron, nickel, or rhodium). Cobalt has rarely been used as a model catalyst, although foils and single crystals of the metal are readily available. One reason, perhaps, is the difficulty in removing impurities from its bulk, although the cleaning of iron presents a more formidable challenge.

The purpose of this paper is to use cobalt as a model catalyst for combined reactivity and surface science studies of its behavior for the CO–H_2 reaction. We used both polycrystalline cobalt foils and thin cobalt films deposited on gold foils as small-area model catalysts. As will be seen, the thin cobalt films proved to have catalytic properties different from those of the clean cobalt foils. The rates at 101 kPa, product distribution, activation energy, and partial pressure dependencies were determined for the CO hydrogenation reaction. These kinetic parameters were then compared with that of iron, nickel, and rhodium.

Carbon monoxide hydrogenation has previously been studied on Co(0001) (*3*), Co(11$\bar{2}$0), Co(10$\bar{1}$2) (*4*) and on submonolayer coverage of cobalt on W(110) and W(100) (*5*). Supported cobalt catalysts have been studied frequently, and we have used the results of Johnson *et al.* (*5*), Vannice

[1] Laboratory of Physics, Helsinki University of Technology, 02150 Espoo, Finland

[2] Corrosion Research Laboratory, Sumitomo Metal Industries, Ltd. 8, 1, Fusoh-Cho, Amagasaki, Japan, 660.

[3] To whom all correspondence should be addressed

0021-9517/93 $5.00

(6), and Fu and Bartholomew (7) for comparisons.

Our studies show an activation energy for methane formation on polycrystalline cobalt of 86 kJ/mol based on the initial rate of methane formation. The activation energy on cobalt single crystals is lower (70 kJ/mol) (4), but higher on strained cobalt surfaces (93 kJ/mol) (5).

Cobalt shows a lower activation energy than Rh, Ni, and Fe. The turnover rates can be arranged into two groups: Fe and Co show higher rates than Ni and Rh and the selectivity towards methane decreases in the order Ni > Rh > Co > Fe. According to the measurements on supported catalysts (6), the ranking for activation energy is Fe < Rh < Ni < Co, and for turnover rate Fe > Ni > Co > Rh, indicating that the support material may alter the activity and the reaction mechanism.

Since only low-molecular-weight C_1–C_4 hydrocarbons are produced at the low conversion rate obtained on our small-area model catalysts, the formation of liquid hydrocarbons from CO and H_2 (that cobalt is so well known for) must be the result of secondary reactions similar to the behavior of iron.

2. EXPERIMENTAL

All of our research was carried out in a combined ultrahigh vacuum (UHV) atmospheric pressure chamber used, e.g., by Garfunkel *et al.* (8) and described originally by Cabrera *et al.* (9). The camber is pumped with a diffusion pump and it is equipped with double-pass cylindrical mirror analyzer (CMA) for Auger electron spectroscopy (AES) and a 3-keV sputter ion gun for sample cleaning. A quadrupole mass spectrometer can be used to perform thermal desorption spectroscopy and vacuum diagnosis.

For catalytic reaction rate studies the sample that is placed inside the UHV chamber on a manipulator can be enclosed in a special isolation cell that constitutes part of a microbatch reactor operating at atmospheric pressures. The isolation cell is closed by a hydraulic piston that presses a standard mini ConFlat Cu gasket between two knife edges. While the pressure inside the cell is raised to 101 kPa (760 Torr), the pressure outside the cell is maintained below a few μPa (below 10^{-8} Torr). Other parts of the reaction loop are a gas chromatograph (GC), automatic sampling valve, and a teflon pump by which the gas mixture is circulated inside the reaction loop. The total volume of the reaction loop is approximately 260 cm^3. The temperature of the tube walls can be raised with heating tapes to prevent condensation of reaction products during the run. Products generated during the reaction experiment are separated with the GC using a Porapak Q column, and measured with a flame ionization detector. The evacuation of the cell after a reaction experiment before opening the cell to the vacuum chamber is performed with a mechanical pump and then with a sorption pump until the pressure is below 200 mPa (1.5 mTorr).

The reactants are introduced via a gas-handling manifold pumped with the mechanical and the sorption pump. The gas pressure during introduction is measured with a differential pressure gauge. All gases in the experiments are passed through liquid nitrogen cooled molecular sieve traps prior to use. The CO (99.5%) was first trapped by the cold (77 K) molecular sieve and then released by removing the LN_2 dewar to let the trap temperature increase about 10 K. This is enough to exceed the boiling point of CO (81.6 K) but to remain still below the boiling points for e.g., O_2 (90 K), CO_2 (195 K), or methane (109 K). Argon (99.9%) was introduced in similar manner when it was needed as a fill-up gas. In the case of hydrogen (99.99%) it is passed through the cold trap with continuous cooling of the trap.

Two kinds of samples were used in the experiments; cobalt thin films evaporated on gold foils and thin cobalt foils. The gold substrates used in the experiments were small rectangular pieces of 38-μm-thick foil about 1 cm^2 in size and the cobalt foils were 125-μm-thick high-purity foil with surface

areas $<1 cm^2$. Both types of samples were spotwelded on 0.9-mm Au wires connected to a rotatable manipulator using Cu supports. This way the sample could be resistively heated without significant heating of any other part of the chamber. During reaction rate studies when typical currents of 40 A were used the Cu feedtroughs were cooled by air flow. The sample temperature was measured via a chromel–alumel thermocouple spotwelded on the backside of the sample, and maintained using a proportional temperature controller within ± 3 K. At the start of the reaction experiment the sample temperature was raised during a 90 s time span.

Prior to experiments both faces of both types of samples (cobalt and gold foil) were cleaned. The gold substrates were cleaned using cycles of Ne^+ or Ar^+ sputtering followed by O_2 exposure at 770 K until only gold peaks could be detected. The cobalt was then evaporated on the clean gold surface. After reaction experiments, the surface was cleaned by short sputtering in order to remove carbon deposited during the reaction, which in most cases required the removal of the rest of the cobalt layer as well. The cobalt foil samples were cleaned by Ar^+ sputtering followed by H_2 exposure at 101 kPa for several hours to react with the carbon segregating to the surface. This produced a cobalt surface with small amounts of Cl that was easily removed by sputtering. When the surface was annealed after sputtering, small amounts of carbon segregated to the surface. After the reaction rate measurements the surface was cleaned by sputtering followed by annealing at 770 K.

The cobalt evaporation source consists of a 0.5-mm W-wire around which the high purity cobalt was wrapped. The source is surrounded by a Ta shield to prevent cobalt deposition all over the chamber and the amount of metal deposition is controlled by manual shutter in front of the source. The current through the W-wire was manually adjusted and a Pt–Re thermocouple was used to measure its temperature. The current feedtroughs were cooled by air flow. The pressure in the UHV chamber during cobalt evaporation was below 1 μPa.

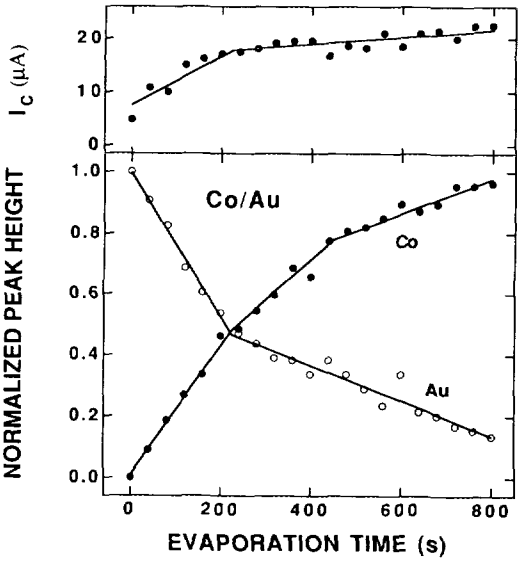

FIG. 1. Auger peak intensities of Au NVV (239 eV) and Co LMM (775 eV) lines and the secondary emission current due to Auger electron gun (I_c) as a function of cobalt evaporation time on Au foil. The Auger peak intensities have been normalized independently.

3. RESULTS

3.1. Cobalt Deposition onto Gold and Its Subsequent Diffusion into the Substrate

Cobalt evaporation was performed at room temperature, and was monitored by measuring the cobalt and gold Auger signals versus evaporation time (As–t) and the secondary emission current due to Auger electron gun versus evaporation time (I_c–t) as shown in Fig. 1. The shapes of the As–t and I_c–t curves give information on the layer growth mechanism. Discontinuous changes (or break points) in the slopes are usually assigned to completion of adsorbate layers. The solid lines have been drawn to determine the changes in the slopes of the curves in Fig. 1. Both As–t signals indicate break points at about 225 s that can be assigned to the completion of the first monolayer. The second break at 450 s that can be seen

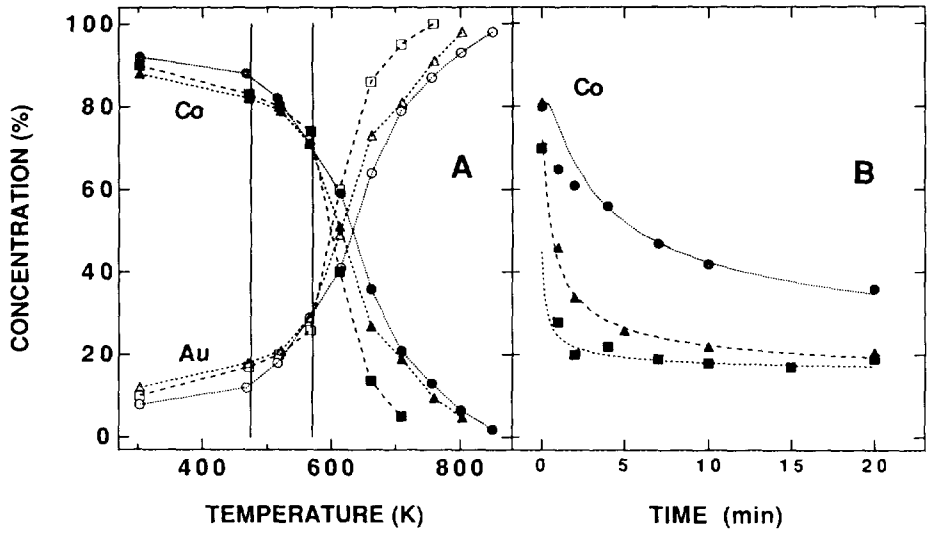

FIG. 2. The relative amounts of cobalt (black) and gold (open) on the surface as a function of annealing temperature (A) and as a function of annealing time (B) in vacuum. The amounts have been calculated from Auger intensities measured at room temperature between subsequent annealings. (A) The markers correspond to annealing times of 2 (○), 10 (△), and 20 min (□). The vertical lines indicate the range of reaction temperatures used in this work. (B) The markers correspond to annealing temperatures of 580 K (○), 620 K (△), and 670 K (□). The lines are fits to the data using Eq. (1) with diffusion coefficient values 4×10^{-17}, 2.5×10^{-16}, and 7×10^{-16} $cm^2 s^{-1}$ at 580, 620, and 670 K, respectively.

only in the cobalt data indicates where the second monolayer would be completed if the growth proceeded in layer-by-layer mode. The Au Auger peak intensity after 225 s evaporation is about 50% of that of the initially clean surface. For higher evaporation times no clear break points can be seen in the data and the curves smoothly reach their saturation values, though the solid lines are drawn as the growth would proceed in layer-by-layer mode.

In Fig. 2A the effect of temperature on the amount of Co and Au in the surface layer is displayed. The Co and Au Auger peak intensities were measured as a function annealing temperature from 300 to 900 K with 2, 10, and 20 min annealing at each temperature. The initial thickness of the cobalt layer was about 6–8 ML. The data indicates that cobalt diffusion into gold becomes detectable upon heating to 600 K in vacuum. The binary phase diagram of Au–Co system (*10*) indicates 0.1 wt% solubility of cobalt in gold at 670 K.

The diffusion of cobalt into gold was further studied by isothermal annealing of the as deposited cobalt film at 580, 620, and 670 K in vacuum. The data from these experiments is shown in Fig. 2B. The measured data was fitted using the equation

$$I(t) = I_0 \operatorname{erf}\left(\frac{x_0}{2\sqrt{Dt}}\right), \qquad (1)$$

where t is time, x_0 is the information depth (about 12 Å using AES), and D the diffusion coefficient. Equation (1) has been obtained from the solution of Fick's diffusion equation assuming diffusion only in one dimension (*11*). The values for the diffusion coefficient were 4×10^{-17}, 2.5×10^{-16}, and 7×10^{-16} $cm^2 s^{-1}$ at 580, 620, and 670 K, respectively, when an information depth of 12 Å was assumed. These values give an esti-

mated activation energy of 92 kJ/mol for cobalt diffusion into gold.

The diffusion of cobalt into gold was also observed during the CO hydrogenation reaction at reaction temperatures between 475 and 570 K. To characterize the amount of cobalt diffused into gold and the speed of the process, we measured the surface composition before the reactions and after 1, 2, and 10 min at the reaction conditions (101 kPa total pressure and 1.24 H_2/CO ratio). The final cobalt surface composition was already reached after 2 min at the reaction conditions. The rate of diffusion increased when the reaction temperature increased but some diffusion was also seen after reaction rate studies at 475 K. The cobalt film thickness before the reaction was about 6–8 ML and after the reaction experiment it had been reduced to below 1 ML.

The cobalt evaporation was repeated several times followed by annealing of the surface up to 670 K in order to slow down the diffusion by increasing the cobalt concentration in the near surface region of the gold foil. This resulted in slower cobalt diffusion and a little higher cobalt concentrations of the surface after the reaction rate experiments but during all the reaction rate studies we lost considerable amount of cobalt. To characterize the driving force for cobalt diffusion into the gold a set of runs were performed in 101 kPa where first H_2, then CO, and finally both were replaced by argon. Cobalt diffusion into gold was observed only in the case where H_2 was present.

The amount of cobalt on the surface before and after reaction experiments was analyzed using AES. Because the information depth of AES is several monolayers, the cobalt signal does not necessary give the surface coverage of cobalt on gold. The coverage calculated from Au NVV and Co LMM Auger peak intensities were, however, used when the turnover rates on Co/Au system were calculated. We also performed a few thermal desorption studies on Co/Au samples. First CO was adsorbed at room temperature and then the desorbed amounts were used to estimate the coverage of cobalt after the reaction. The results indicate that the values obtained for cobalt coverages from the AES data after the reaction are about a factor of 2 too high. This discrepancy may be due to different information depths or to carbon deposits on the surface that block cobalt sites from CO adsorption.

3.2. Carbon Monoxide Hydrogenation on Co/Au System

The catalytic hydrogenation of carbon monoxide has been investigated in the temperature range from 475 to 570 K on cobalt films evaporated on gold. As described in the previous section the cobalt film thickness during the reaction is below 1 ML due to Co diffusion into Au though the initial thickness of the freshly deposited cobalt layer was 6–8 monolayers. The initial rate of methane formation for the Co/Au surface was 0.02 methane molecules per cobalt site per second at 550 K when the H_2/CO ratio was 1.24 and the total pressure 101 kPa (760 Torr). At 525 K with H_2/CO ratio of 3 the rate equals 0.01 CH_4 site^{-1} s^{-1}. The initial rate of methane formation was determined by evaluating the initial slope of the accumulated methane versus time curve and dividing it by the estimated number of cobalt atoms on the surface. The amount of cobalt on the surface after the reaction was estimated from the AES Co and Au peak heights measured immediately after the reaction.

The initial reaction rate as a function of the inverse temperature is plotted in Fig. 3A. The data has been obtained by varying the sample temperature while holding the total pressure and reactant gas composition constant at P_{H_2} = 56 kPa (420 Torr) and P_{CO} = 45 kPa (320 Torr). The activation energy for methane formation determined from the initial reaction rates was (92 ± 10) kJ/mol with a tendency to decrease as the reaction time increases. In Fig. 3B we plot the methane and ethene concentrations after 1 h reaction time as a function of the inverse temperature. At this point the activation energy was estimated to (86 ± 7) kJ/mol for

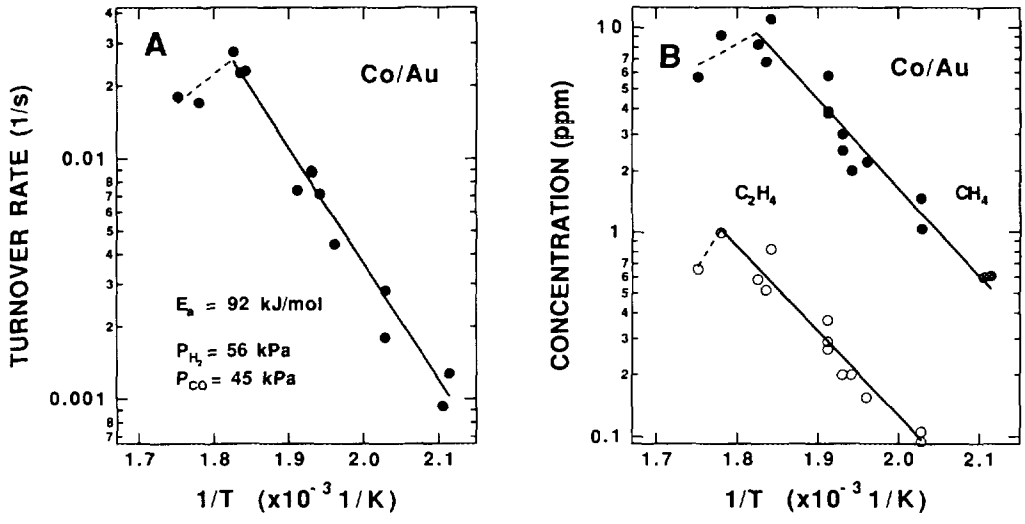

FIG. 3. Initial rate of methane formation (A) and the accumulated amount of C_1–C_3 products after 1 h reaction (B) as a function of inverse temperature on Co/Au samples. The H_2/CO ratio was 1.24 and the total pressure 101 kPa (760 Torr). The solid line in (A) is drawn for an activation energy of 92 kJ/mol, whereas the solid lines in (B) are obtained with values of 86 kJ/mol for methane and 79 kJ/mol for ethene.

methane and (79 ± 9) kJ/mol for ethene. The data in Fig. 3 fall relatively well on the lines representing the activation energies except at temperatures exceeding 560 K where the activity starts to decrease.

The product distributions at different temperatures after 1 h reaction time are given in Fig. 4. The total pressure was 101 kPa and the H_2/CO ratio 1.24. At 475 K the reactivity is so small that formation of longer chain hydrocarbons could not be detected but the selectivity shifts towards higher molecular weight hydrocarbons with increasing temperature. Between 495 and 550 K the selectivity to methane is between 87 and 85%, but at 570 K it is only 68%. The Co/Au surface is highly selective toward alkenes under these conditions and no C_2–C_3 alkanes were detected.

The dependence of the rate of methane formation on the partial pressure of the reactants was determined by varying the partial pressures of both reactant gases independently while maintaining the total pressure at 101 kPa using argon as a fill-up gas. The results from these experiments

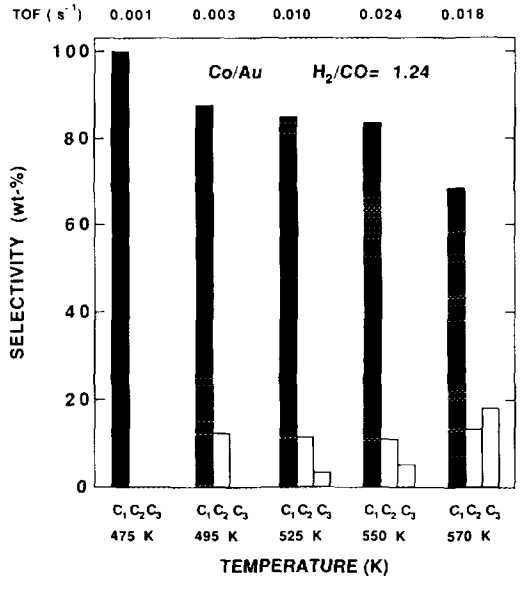

FIG. 4. Product distributions at five different temperatures on Co/Au surface. The total pressure was 101 kPa and the H_2/CO ratio 1.24. The initial reaction rate is also given at these temperatures. The saturated hydrocarbons are represented by black columns, whereas unsaturated are denoted by white.

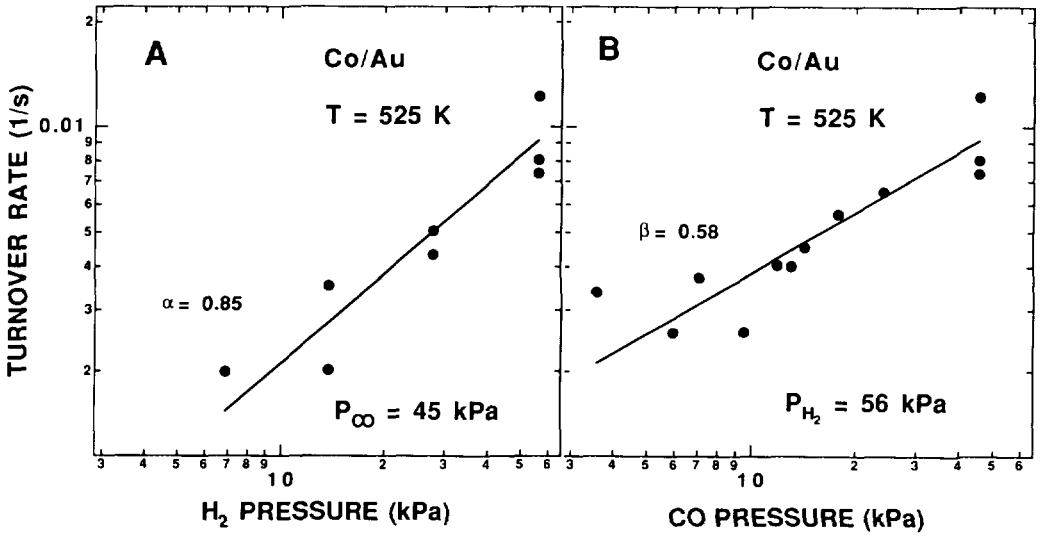

FIG. 5. Hydrogen (A) and carbon monoxide (B) partial pressure dependence on the rate of methane formation on Co/Au surface. The reaction temperature was 525 K and the total pressure was 101 kPa.

performed at 525 K are shown in Fig. 5. The measured data was fitted to the equation

$$r_{CH_4} = k\, p_{H_2}^{\alpha} p_{CO}^{\beta} \qquad (2)$$

to determine the coefficients α and β for H_2 and CO pressure dependencies. The lines in Fig. 5 correspond to values of $\alpha = 0.85$ for H_2 pressures between 6.8 and 56 kPa while CO pressure was 45 kPa, and $\beta = 0.6$ for CO pressure from 3.5 to 45 kPa while H_2 pressure was 56 kPa.

After termination of the reaction and evacuation of the cell the sample surface was characterized by AES to detect possible impurities, the amount of carbon deposited on the surface during the reaction and to estimate the amount of cobalt left on the surface. After some of the runs small contamination of chlorine was detected on the surface. The source of Cl is most probably the previous reactions that used chlorinated hydrocarbons in the same system. The accumulation of carbon on the Co/Au surface is demonstrated in Fig. 6, where the carbon-to-cobalt AES peak intensity ratio is plotted as a function of reaction temperature. The data indicate that the ratio starts to increase at temperatures higher than 525 K. If we assume an equal depth distribution for Co, C, and Au atoms after the reaction experiment, we get typical concentrations of 20%

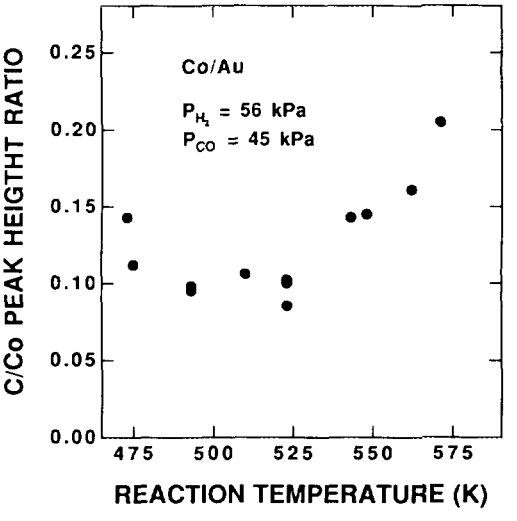

FIG. 6. The carbon/cobalt AES peak height ratio as a function of reaction temperature on Co/Au samples. The data has been measured immediately after evacuation of the reaction cell. The gas composition used featured an H_2/CO ratio of 1.24 at 101 kPa.

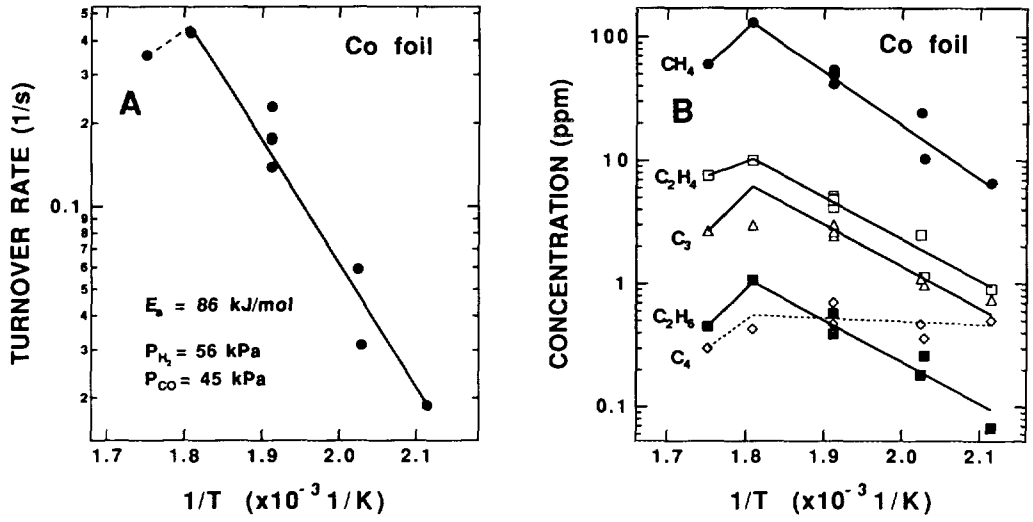

FIG. 7. Initial rate of methane formation (A) and the accumulated amount of C_1–C_4 products after 1 h reaction (B) as a function of inverse temperature on cobalt samples. Ethane and ethene are shown separately and C_3 and C_4 are propene and butene, respectively. The H_2/CO ratio was 1.24 and the total pressure 101 kPa. The solid line in (A) is drawn for an activation energy of 86 kJ/mol, whereas the solid lines in (B) are obtained with values of 83 kJ/mol for methane, 65 kJ/mol for ethene, 68 kJ/mol for ethane, 63 kJ/mol for propene, and 5 kJ/mol for butene.

Co and 2% C on the gold surface, indicating that only every tenth cobalt atom is decorated with carbon.

It should be pointed out that in case of segregation of gold onto the cobalt surface, or of carbon, we cannot assume equal depth distribution for these three elements. In this circumstance the surface concentrations obtained using the assumption of equal depth distribution would have to be modified.

3.3. Carbon Monoxide Hydrogenation over Cobalt Foils

For comparison, all the CO hydrogenation experiments performed on the Co/Au system were repeated on cobalt foil samples in the temperature range of 475 to 570 K. The initial rate of methane formation at 550 K when the H_2/CO ratio was 1.24 and the total pressure 101 kPa was 0.43 methane molecules produced per cobalt site per second. After increasing the H_2/CO ratio to 3 and decreasing the reaction temperature to 525 K the initial rate remained almost equal, 0.52 CH_4 site^{-1} s^{-1}. The geometrical surface area of the sample with 10^{15} atoms/cm^2 was used to estimate the initial turnover number from the accumulated methane versus time data.

The Arrhenius plots for the CO hydrogenation is plotted in Fig. 7. The data has been obtained by varying the sample temperature while holding the total pressure and reactant gas composition constant (P_{H_2} = 56 kPa, P_{CO} = 45 kPa). The solid line in the initial methane formation rate data in Fig. 7A represents an activation energy of 86 kJ/mol. In Fig. 7B the concentration of C_1–C_4 products after 1 h reaction time is plotted. The activation energy for methane formation when determined from the data taken after 1 h reaction time is (83 ± 4) kJ/mol. The activation energies for ethene, ethane, and propene formation were estimated to be (65 ± 7), (68 ± 7), and (63 ± 10) kJ/mol, respectively. The amount of butene formed seems to depend only weakly on temperature.

The product distributions after 1 h reaction time at various temperatures are given

in Fig. 8. The saturated hydrocarbons are marked with black and the unsaturated with white columns. It can be seen that the selectivity towards methane increases from 55 to 71% with increasing reaction temperature up to 550 K. The 570-K case seems to deviate from this overall trend by lower methane formation. The C_2 fraction remains almost constant and the C_3 and C_4 fractions decrease with increasing temperature up to 550 K. The fraction of ethene in C_2 is between 86 and 94% and the C_3 and C_4 hydrocarbons are solely alkenes.

The dependence of the rate of methane formation on the partial pressures of the reactants was determined by varying the partial pressure of both reactant gases independently while maintaining the total pressure at 101 kPa using argon as a fill-up gas. The results from these experiments performed at 525 K are shown in Fig. 9. For CO pressure dependence measurements the H_2 pressure was held at 56 kPa (420 Torr) and for the H_2 pressure dependence measurements the CO pressure was held at 25 kPa (190 Torr). The solid lines in the initial rate data in Figs. 9A and 9B have been obtained using Eq. (2) with exponents $\alpha = 1.5$ and $\beta = -0.75$ for H_2 pressures between 12 and 76 kPa and for CO pressures from 3.5 to 45 kPa, respectively. The partial pressure dependencies of all products are given in Figs. 9C and 9D after 1 h reaction time. The concentrations of all the products increase with increasing H_2 pressure, and decrease with increasing CO pressure with the exception of ethene and propene at CO pressures between 3.5 and 7 kPa. The lines in Figs. 9C and 9D have also been obtained using Eq. (2) with the values given in Table 1.

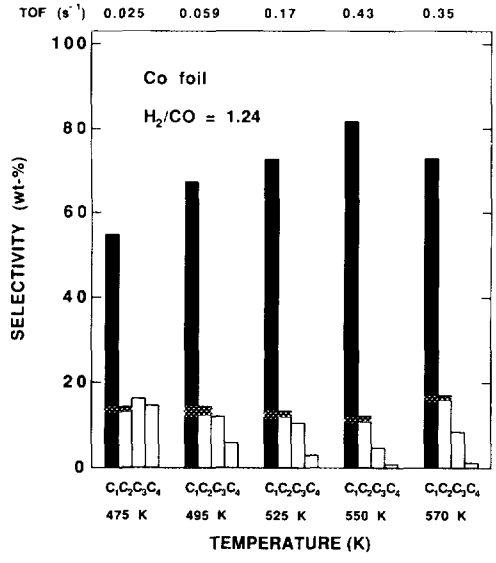

FIG. 8. Reaction product distributions at five different temperatures on cobalt foil. The total pressure was 101 kPa and the H_2/CO ratio 1.24. The initial turnover rate is also given at these temperatures. The C_2 is mainly ethene; C_3 and C_4 are propene and pentene, respectively. The saturated hydrocarbons are represented by black columns, whereas unsaturated are denoted by white.

To further characterize the dependence of the reaction rate on the reactant gas mixture the H_2/CO ratio was changed and product distributions plotted in Fig. 10 after 1 h reaction time at 525 K. The relative amount of methane produced increases, the C_2 and C_3 fractions decrease and the C_4 fraction remains constant as the H_2/CO ratio increases. The ethene fraction of C_2 products decreases from 92 to 73% when the H_2/CO ratio goes from 1.24 to 3. The total activity of the cobalt foil increases and the amount of carbon detected on the surface after the reaction decreases with increasing H_2/CO ratio.

The cobalt foil surface composition was characterized by AES immediately after opening the reaction cell without any further heating of the sample. The spectra showed variable amounts of carbon deposited on the surface together with random appearance of small S or Cl peaks. The AES peak intensity ratio of carbon and cobalt after the reaction is plotted in Fig. 11 as a function of reaction temperature. The C/Co ratio stays almost constant as the temperature increases up to 525 K. At 550 K the amount of carbon is slightly higher and at 570 K significantly more carbon has been deposited on the surface during the reaction which also decreased the cobalt peak height. The peak shape of the carbon KLL Auger lines (*12*) indicates that only after reaction experiments at 570 K carbon is in graphitic form.

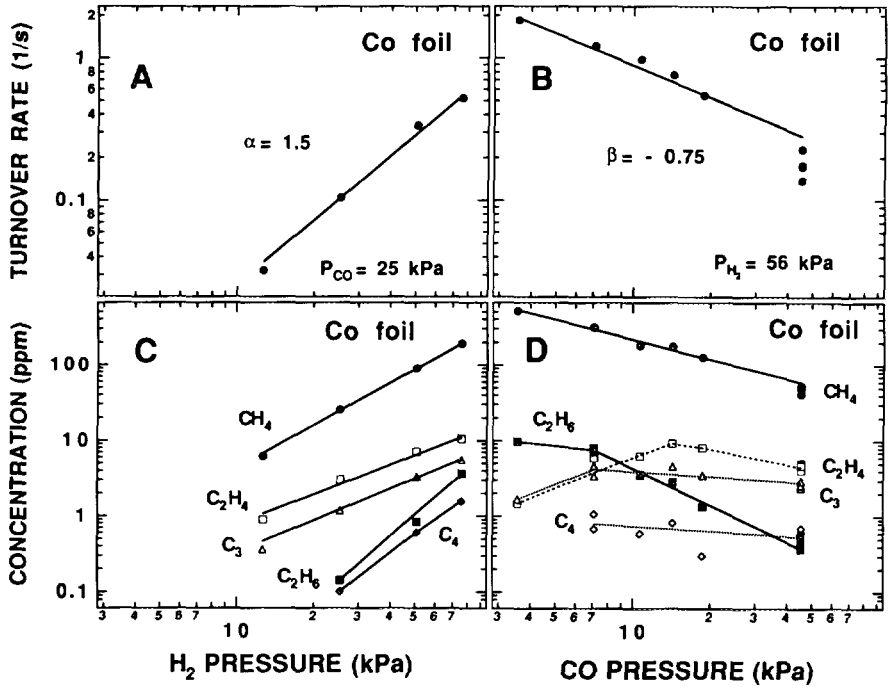

FIG. 9. The partial pressure dependence of initial rate of methane formation (A, B) and of accumulated products after 1 h reaction time (C, D). Hydrogen partial pressure dependences are given in (A) and (C) and carbon monoxide partial pressure dependences in (B) and (D). The reaction temperature was 525 K and the total pressure was 101 kPa.

When the amount of products was plotted as a function of carbon number in the hydrocarbon chain, the value for the chain growth probability α was obtained using the Anderson–Schultz–Flory distribution. For cobalt foil a value of 0.28 was obtained for H_2/CO ratio of 3 after 2 h reaction time. The experiment was continued up to 5 h but only minor changes in the product distribution were detected that did not affect the value of α.

TABLE 1

Hydrogen (α) and Carbon Monoxide (β) Partial Pressure Exponents of the Reaction Rate of Different Reaction Products on the Cobalt Foil Surface

	CH_4	C_2H_4	C_2H_6	C_3	C_4
α	1.87	1.30	2.9	1.4	2.5
β	−0.86	—	−1.6	−0.21	−0.21

Note. The data have been measured after 1 h reaction time and are shown in Figs. 9C and 9D.

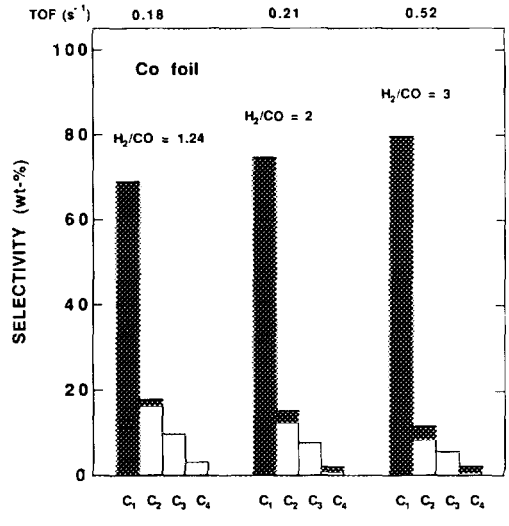

FIG. 10. Product distributions for reactions at different H_2/CO ratios at 525 K at 101 kPa total pressure. The saturated hydrocarbons are represented by black columns, whereas unsaturated are denoted by white.

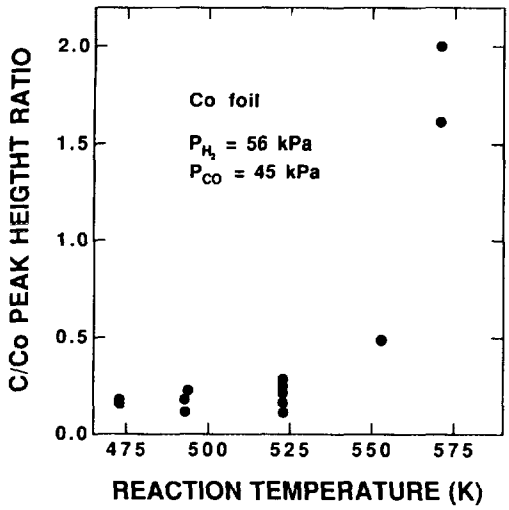

FIG. 11. The amount of carbon on the surface after reaction measured by AES as a function of reaction temperature. The total pressure was 101 kPa and the H_2/CO ratio was 1.24.

4. DISCUSSION

4.1. Cobalt Film Growth and Cobalt Diffusion in Gold

The Auger signal versus time plot in Fig. 1 showed one break point that was assigned to completion of the first monolayer. This film growth data is not sufficient for any firm conclusion of the growth mode, but we assume that the cobalt layer on gold grows at room temperature by completion of the first monolayer after which a three-dimensional growth begins. The Co/Au peak height ratio at 1 ML (monolayer) is about 3.6 which gives a cobalt concentration of 34% when using sensitivity factors for cobalt and gold (*12*). The layer growth information is only used to estimate the film thickness before and after the reaction experiments.

Our results of the film growth can be compared to cobalt deposition studies on other metals. Deposition of cobalt on Pt(100) at room temperature gives rise to interdiffusion of Co and Pt with the loss of the LEED pattern after 1 ML (*13*). When the evaporation is performed at lower temperature (100 K) on reconstructed Pt(110)(1 × 2) surface, pseudo-layer-by-layer growth has been observed without any long range order (*14*). Epitaxial layer-by-layer growth has been reported on Cu(100) between 270 and 450 K (*15, 16*). On Mo(110) cobalt films follow pseudo-layer-by-layer growth at RT with a tendency to begin the formation of the next layer before the previous is completed (*17*). Completion of each layer before the start of the next can only be achieved by deposition or annealing at elevated temperatures. No alloying can be seen up to 1 ML. On gold substrates only chromium has been studied. On Au(100) the first Cr layer grows epitaxially and the next layer can grow either in layer-by-layer mode or three dimensionally (*18*).

The annealing studies in vacuum give an estimated activation energy for cobalt diffusion in gold of 92 kJ/mol. Cobalt diffusion in gold has been studied earlier in the temperature range between 490 and 512 K (*19*) and between 970 and 1320 K (*20*). The low-temperature-range data has been obtained using X-ray photoelectron spectroscopy from a layer structure consisting of 300 nm of Au on 40 nm of Co on a quartz substrate. The cobalt diffused through the gold layer is measured after heating in air between 490 and 512 K. The reported activation energy of 109 kJ/mol for cobalt diffusion is consistent with the grain boundary diffusion mechanism according to Swartz *et al.* (*19*). The high temperature range data has been obtained using X-ray diffraction. In this temperature range the activation energy is considerably higher than at low temperatures, 184 kJ/mol (*20*), but values for diffusion coefficient extrapolated to the lower temperature range coincide with our values. A summary of the values for diffusion coefficients between 470 and 570 K is given in Table 2.

Cobalt diffusion into gold was observed to take place at much lower temperatures when the samples were heated in a hydrogen atmosphere. The temperature needed for reaching the same surface composition in 10 min decreases from 700 to 525 K. After

TABLE 2

Comparison of Diffusion Coefficient Values for Cobalt Diffusion in Gold between 470 and 570 K

T(K)	D(cm^2 s^{-1})	D(cm^2 s^{-1})	D(cm^2 s^{-1})
470	*7.2×10^{-19}	*8.8×10^{-22}	3.9×10^{-16}
580	4.0×10^{-17}	*3.3×10^{-18}	*5.1×10^{-14}
670	7.0×10^{-16}	*1.1×10^{-15}	*1.6×10^{-12}
Reference	This work	(20)	(19)

Note. The extrapolated values are denoted with an asterisk[*].

heating to 525 K in an H_2 atmosphere, the surface composition includes about 20% cobalt in the near-surface region, whereas the annealing experiments in vacuum at 700 K ended up in a state where no cobalt was left on the surface. Thus the H_2 atmosphere seems to affect the surface region but cannot push the cobalt atoms deeper into the gold bulk.

4.2. *Comparison of CO Hydrogenation Results on Co/Au and on Cobalt Foil*

The most obvious difference observed in the reaction experiments between the Co/Au system and the cobalt foil is the about 20-fold difference in the total methane formation rate. On clean gold no reactivity was observed indicating that the presence of cobalt atoms is essential. The amount of cobalt on the surface has been taken into account when the turnover rates were calculated and thus the loss of cobalt during the reaction is not sufficient to explain the difference in the rates.

The following remarks and possible explanations can be made based on the measured difference in the rates: The difference indicates that only about 5% of the surface sites are active in the reaction on Co/Au surface compared to cobalt foil, the active Co site is not the on-top site but the reaction requires more than one Co atom, and/or sites with Co–Au bond are active in the reaction with lower activity than the sites on clean cobalt.

In order to test the active site hypothesis, we calculated the fraction of bridge and threefold sites as a function of cobalt island size assuming a hexagonal surface and a cobalt concentration of 20%, as was typically given by AES after the reaction. The results indicate that if the reaction requires bridge or threefold cobalt sites, the presence of small (<5 atoms) cobalt islands on gold could explain the difference in the rate of methane formation between Co foil and Co/Au. If the surface was covered with a gold or carbon monolayer marked attenuation of the reaction rate would occur as well. Future studies will have to verify the correlation between the surface composition and reactivity.

The activation energy for methane formation on Co/Au system is higher than that on cobalt foil though they can be regarded equal within the experimental error as can be seen in Table 3. On both surfaces the activation energy based on the initial rate measurements is 3–4 kJ/mol higher than that based on the steady-state data. The activation energy for ethene formation on Co/Au is higher than that observed on cobalt foil indicating a different rate-limiting step for ethene formation.

The product distributions at different tem-

TABLE 3

Comparison of CO Hydrogenation Data on the Co/Au System and on Cobalt Foil

	Co/Au	Cobalt
CH_4 turnover rate at 550 K (site^{-1} s^{-1})	0.02	0.43
Activation energy for CH_4 formation (from the initial rates)	92 ± 10	86 ± 7 kJ/mol
Activation energy for CH_4 formation (from the steady state rates)	86 ± 7	83 ± 4 kJ/mol
Hydrogen pressure exponent at 525 K	0.85 ± 0.2	1.5 ± 0.1
CO pressure exponent at 525 K	0.6 ± 0.15	−0.75 ± 0.2
Activation energy for C_2H_4 formation	79 ± 9	65 ± 7 kJ/mol

Note. The total pressure was 101 kPa and the H_2/CO ratio 1.24 except for the partial pressure dependence measurements.

peratures given in Figs. 4 and 8 show an opposite trend as the temperature increases. In the Co/Au case the fraction of methane decreases with increasing temperature, whereas on cobalt foils it increases. The decreasing methane fraction is explained by the increasing total activity of the Co/Au foil as the temperature increases. At 470 K the total activity is too small to produce detectable amounts of hydrocarbons other than methane but as the temperature increases longer chain hydrocarbons are also formed. On the cobalt foil longer chain hydrocarbons are formed and both types of surfaces are highly selective towards alkenes.

The partial pressure dependencies of these two surfaces are remarkably different as can be seen in Figs. 5 and 9 and in Table 3. The hydrogen exponents are 0.85 and 1.5 and the CO exponents 0.6 and −0.75 for Co/Au and cobalt foil, respectively. From these values we can deduce that on cobalt foil the reaction may use all the hydrogen that is available and too large amounts of CO inhibit the reaction. On the contrary, on the Co/Au system the adsorption of both reactants are equally needed to produce methane.

In order to characterize the difference between the Co/Au and cobalt foil samples, the partial pressure data was used to determine the reaction mechanism for methane formation on these surfaces. On transition metal surface the CO hydrogenation has been proposed to proceed either via CO dissociation or via formation of the enol (CHOH) complex on the surface (*21*, *22*). We were able to explain all partial pressure dependencies using either of these reaction models, but reasonable fits and surface coverages lead us to conclude that on cobalt foil the reaction proceeds via CO dissociation and the rate-limiting step is CH_3 hydrogenation as reported earlier (*3*). On Co/Au the rate limiting step is either CHOH or CH_2 formation within the enol-complex model. The analysis of the reaction mechanism is discussed in more details in the Appendix.

It should be pointed out that we ignored the possibility of changes in surface composition (for example, gold surface segregation on the Co/Au catalyst) of the catalyst as the partial pressures of CO or H_2 are altered. This could complicate the analysis of the experimental data.

4.3. Comparison of Our Results to Other Studies on Cobalt

We have measured a set of parameters on polycrystalline cobalt surface and on the Co/Au system including initial turnover rates, activation energies, and selectivities for different products, and partial pressure dependencies. When these parameters are compared to studies on ordered cobalt surfaces, the following conclusions can be made.

The rate of methane formation obtained in these experiments on polycrystalline foils is a factor of two higher than the rate on Co(0001) single crystals where the turnover frequency of 0.08 site^{-1} s^{-1} has been obtained as an average for 2.5 h experiment at 525 K. The higher activity on cobalt foil is mainly due to the difference in the real surface area of the sample. The Co(0001), Co(11$\bar{2}$0), and Co(10$\bar{1}$2) surfaces (*3*, *4*) showed only a weak structure sensitivity for methane formation and the strained Co/W(100) and Co/W(110) surfaces (*5*) also had about the same turnover rates. Thus we can conclude that cobalt surfaces do not show any strong structure sensitivity in methane formation.

The activation energy for methane formation on Co(0001), Co(11$\bar{2}$0), and Co(10$\bar{1}$2) was reported to be 70 kJ/mol (*4*) and on Co/W(100) and Co/W(110) 93 kJ/mol (*5*). The activation energy measured on polycrystalline foil, E_a = 86 kJ/mol, is located between these two. The differences are not due to different crystal planes, as can be seen in the work of Geerlings *et al.* (*4*). One possible explanation is the difference in the amount of carbon deposited on the surface, which is known to lower the activation energies on cobalt surfaces (*23*, *21*). On strained Co/

W surfaces, on the other hand, the activation energy can be higher because of surface structures uncommon to cobalt. On supported cobalt catalysts activation energies ranging from 86 to 150 kJ/mol (*5*) and from 90 to 130 kJ/mol (*7*) have been reported, depending on the metal loading and the extent of reduction. The reported values measured in Co/Al_2O_3 systems by Vannice (*6*) (113 ± 18 kJ/mol) and Agrawal *et al.* (*21*) (117 kJ/mol) lie within these limits. The observations by Lee and Bartholomew (*22*) for Co/Al_2O_3 explain the wide variations in the activation energies in the supported catalysts; and indicate on bulk cobalt a value of (81 ± 2) kJ/mol for the activation energy. This agrees well with our data.

The activation energies for longer chain hydrocarbon formation on cobalt are 65, 68, and 63 kJ/mol for ethene, ethane, and propene formation, respectively. These values agree fairly well with the value of 70 kJ/mol reported by Geerlings *et al.* on Co(0001) for ethane and propane formation (*3*) and on Co(11$\bar{2}$0) for ethane formation (*4*), indicating that they are formed via the same mechanism on all cobalt crystal planes.

The Co(11$\bar{2}$0) surface produces longer hydrocarbon chains with higher selectivity than Co(0001) or Co(10$\bar{1}$2) surfaces (*3*, *4*). On Co(11$\bar{2}$0) post-reaction spectroscopy with EELS revealed larger amounts of C–C and C–H species on the surface as compared to Co(0001) and Co(10$\bar{1}$2). The zigzag troughs on Co(11$\bar{2}$0) are reported to be responsible for longer hydrocarbon formation (*24*). Our measured product distributions on polycrystalline cobalt are between those measured on Co(0001) and Co(11$\bar{2}$0). Because the surface of the polycrystalline foil consists of different crystal planes, it is expected that the selectivity is between that of a close packed and more open surface like our results show. These results indicate that the chain growth probability is sensitive to the surface structure.

The alkene fraction of C_2 products after 5 h reaction on Co(0001) is 18% (*3*) and on Co(11$\bar{2}$0) 60% (*4*). On Co/W(100) the C_2 alkene fraction is 75% (*5*), and our data indicates a value of 82% under similar conditions. Also on supported cobalt the alkene fraction of C_3–C_7 products is higher than 50% (*5*), indicating that cobalt is a good catalyst for the production of unsaturated hydrocarbons.

The partial pressure dependence on cobalt catalysts can only be compared to values measured on supported catalysts. On Co/Al_2O_3, the hydrogen exponent in Eq. (2) has values 0.5 (*21*) or 1.22 (*6*). The latter agrees with our $\alpha = 1.5$ on cobalt foil. The CO exponent for a fresh catalyst has been reported to be −0.24 (*21*) and −0.48 (*6*) and for a carbon-deactivated catalyst +0.3 (*21*). Our value of $\beta = -0.75$ indicate stronger CO pressure dependence on cobalt foil than on supported cobalt.

4.4. Comparison of Cobalt to Other Transition Metals

Similar CO hydrogenation studies have been performed on Fe(111) (*25*), Fe foil (*26*, *27*, *8*), Ni(100) (*28*), Ni(111) (*29*), Ni foil (*30*), Rh foil (*31*), Rh(111) (*32*), and also on other metal surfaces as reviewed by Rodriguez and Goodman (*33*). When model catalyst studies on cobalt are compared to those on Fe, Ni, and Rh, the following conclusions can be drawn.

Turnover rates and activation energies on Co, Fe, Ni, and Rh can be compared using the collection of the data in Fig. 12 and Table 4. Highest turnover rates for methane formation have been observed on Fe foil where the rate is almost twice to that on cobalt. In this group of four rhodium show the lowest turnover rates. The activation energy on cobalt is lower than that on Fe, Ni, and Rh and it does not correlate with the type of CO adsorption (dissociative on Fe, partially dissociative on Co, and molecular on Ni and Rh (*34*)). High turnover rate and low activation energy explains partially why cobalt has previously been used in the Fischer–Tropsch synthesis.

The activation energies for longer chain hydrocarbon formation are given in Table 5

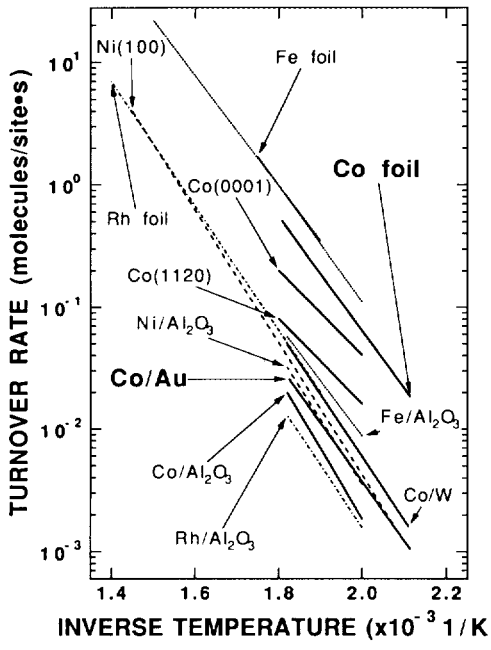

FIG. 12. Turnover rates on different transition metal surfaces as a function of inverse temperature. The H_2/CO ratio is 3 for Co and 4 for Fe, Ni, Rh, and supported catalysts. The total pressure is 101 kPa in all cases except in Rh (92 kPa) and Ni (16 kPa). The data have been obtained from the following references: Co(0001) (*15*), Co(1120) (*16*), Co/W(100) (*18*), Fe foil (*23, 24*), Ni(100) (*26*), Rh foil (*28*), and the supported catalysts (*19*).

for Co, Fe, Rh, Re, and Mo. In most cases the other activation energies are higher than that for methane formation indicating that the rate limiting step for CH_4 formation is different than that for chain growth. The activation energy for ethene formation is equal on Co, Rh, and Fe and that of C_3 products about equal on Rh and on Co. This data indicates that the chain growth proceeds via similar mechanism on all these surfaces.

The partial pressure dependence on small area catalysts has only been studied on Rh (*35*) and on Mo (*36*), and have been used to discuss the reaction mechanism on these surfaces. On cobalt foil the values of the exponents are 1.5 and −0.75, on Rh foil 1.0 and −1.0 (*35*), and on Mo(100) 1.0 and 0.32 for H_2 and CO (*36*), respectively. The reaction mechanism for CO hydrogenation on Ni, Ru, and Fe requires CO dissociation and subsequent hydrogenation of surface carbon (*33, 37*). On the clean Rh surface (*38*) and on Mo(100) (*36*), CO hydrogenation is reported to proceed via CHOH formation. The rate-limiting step is the rupture of the C–O bond after formation of the CHOH-complex. We obtained similar result for the Co/Au system. When the Rh surface was modified with 0.5 monolayer of TiO_x, the exponent values for H_2 and CO changed to 2.5 and −0.3 (*38*). On the modified surface the reaction mechanism changed to the so-called "carbide model" and the rate-limiting step was the adding of the fourth hydrogen atom (*38, 39*), as in our results on clean cobalt. Thus on surfaces, where CO dissociates spontaneously or with the aid of a promoter, the reaction mechanism follows the carbide model whereas on the other surfaces it follows the enol-model.

In supported catalysts the partial pressure exponents of Co, Fe, Ni, and Rh for hydrogen are positive and for CO negative (*6*). The values for the hydrogen exponent of Co (1.22) and Rh (1.04) agree well with those measured on foil samples. Supported Fe shows a value of 1.14 and Ni 0.77, indicating that the selectivity to methane increases with decreasing value of hydrogen exponent.

Cobalt has been predicted to be intermediate between Fe and Ni or Rh in terms of product distribution and carbon deposition during the reaction (*27*). Iron surfaces produce alkenes with high selectivity (79%) until carbon deposition deactivates the catalyst (*26*). On cobalt the selectivity is 75% and graphite formation deactivates the surface if the reaction temperature exceeds 550 K. Nickel surfaces produce only alkanes and graphite formation starts only above 650 K (*28*).

5. CONCLUSIONS

The following conclusions can be drawn from the results and evaluation of the present investigation:

TABLE 4

Methane Turnover Rates, Selectivities to Methane at 525 K, and Activation Energies for Methane Formation for Different Transition Metals

Sample	Pressure (kPa)	H_2/CO ratio	TON $(site\ s)^{-1}$	C_1 (%)	E_a (kJ/mol)	Reference
Co(foil)	101	3	0.33	80	86 ± 10	This work
Co(foil)	101	2	0.21	75	86 ± 10	This work
Co/Au	101	3	0.01	90	92 ± 10	This work
Co(foil)	0.26	40	10	—	71	(30)
Co(0001)	101	2	0.08	80	70	(3)
Co(11$\bar{2}$0)	101	2	0.03	60	70	(4)
Co/W(100)	101	2	0.018	—	93	(5)
Fe(foil)	202	4	8	$68^{540\ K}$	101	(8)
Fe(foil)	600	3	0.4	$85^{573\ K}$	96 ± 8	(26)
Fe(foil)	101	4	0.4	$55^{560\ K}$	88	(27)
Fe(foil) + C	600	3	0.14	$100^{573\ K}$	50 ± 5	(26)
Fe(111)	600	3	—	$70^{573\ K}$	—	(25)
Ni(foil)	0.26	40	0.13	—	71 ± 8	(30)
Ni(100)	16	4	0.012	$93^{503\ K}$	103	(28)
Ni(111)	16	4	0.012	—	103	(29)
Rh(foil)	92	3	0.015	84	100 ± 13	(31)
Rh(111)	600	3	0.02	$90^{573\ K}$	—	(32)
Mo(100)	600	2	0.016	$90^{573\ K}$	100	(36)
Re(foil)	202	4	—	$88^{540\ K}$	117	(8)
Ru(110)	16	4	0.01	—	125	(29)
2% Co/Al_2O_3	101	3	0.0067	$80^{513\ K}$	113	(6)
15% Fe/Al_2O_3	101	3	0.024	$65^{513\ K}$	89	(6)
5% Ni/Al_2O_3	101	3	0.0117	$90^{515\ K}$	105	(6)
1% Rh/Al_2O_3	101	3	0.0049	$90^{538\ K}$	101	(6)

(1) The activation energy for cobalt diffusion into gold in vacuum between 580 and 670 K is 92 kJ/mol. A hydrogen atmosphere was found to enhance the diffusion.

(2) The overall rate for methane formation on Co/Au is a factor of 20 lower than that on cobalt foil. The difference was explained by diffusion of cobalt into gold during the reaction and by assuming that more than one cobalt atom is needed for methane formation on the surface.

(3) The partial pressure dependence on cobalt foil indicates that the reaction proceeds via CO dissociation and that the rate-

TABLE 5

Activation Energies for Hydrocarbon Formation on Transition Metals in kJ/mol

Product	Co	Co	Fe	Rh	Re	Mo
CH_4	86	70	88–100	100	117	100
C_2H_4	65	—	71	65	88	—
C_2H_6	68	70	—	107	—	96
C_3	63	70	—	51	—	—
Reference	This work	(3)	(8)	(35)	(8)	(36)

Note. The total pressure and the H_2/CO ratio varies from one reference to the other.

limiting step is CH_3 hydrogenation. On the Co/Au system the rate limiting step is either formation or dissociation of the CHOH-complex formed without CO dissociation.

(4) Comparison of cobalt foil to cobalt single crystals indicates that methane formation is structure insensitive but the formation of longer chain hydrocarbons is structure sensitive, and has different rate-limiting step than the methane formation.

(5) The activation energy for methane formation on cobalt is (86 ± 4) kJ/mol, which is lower than the activation energies measured of Fe, Ni or Rh.

(6) Graphite formation during CO hydrogenation on cobalt starts above 550 K, which is between the temperatures measured on Fe and Ni (above 650 K).

APPENDIX

Within one reaction mechanism the partial pressure dependencies of the reaction rate can be easily calculated if one elementary reaction step is assumed to be the rate-limiting step (RLS). In the following analysis we used two different reaction mechanisms (*40*, *38*); in Fig. 13A is given the so-called "carbide" model that utilizes CO dissociation and in Fig. 13B the so-called "enol-complex" model where the C–O bond breaking takes place after CHOH formation. Also shown in Figs. 13A and 13B are the reaction rates as functions of H_2 and CO partial pressures when all the steps have been sequentially used as rate-limiting steps. The equations shown in Figs. 13A and 13B were then fitted to the measured partial pressure data shown in Figs. 5 and 9 for Co/Au and cobalt foil, respectively. For an acceptable fit, we required that both H_2 and CO partial pressure dependencies were reproduced with same set of coefficients K_O, K_H, K_{CO}, and K_C.

In the case of cobalt foil data of Fig. 9 we only got acceptable fits using Eqs. (7) from Fig. 13A or 13B, indicating that the CH_3 hydrogenation is the rate limiting step on cobalt foil regardless of the reaction mechanism. The resulting curves from the fits of the carbide model to the cobalt foil data are shown in Fig. 14, where the fit was made to the CO and the parameters were then used to calculate the H_2 partial pressure dependence. The results clearly show that on cobalt foil the rate determining step is the hydrogenation of CH_3 species. The numbers at the lines refer to the different lines in the reaction mechanism equations shown in Fig. 13A.

In the case of Co/Au we got acceptable fits using Eqs. (5) through (7) from Fig. 13A and Eqs. (4) through (7) from Fig. 13B which only excludes the adsorption processes as rate-limiting steps.

The surface coverages during the reaction, θ_{CO}, θ_H, and θ_C, can be calculated as functions of partial pressures when the coefficient K_i are known from the fit. We used the calculated surface coverages to exclude unrealistic results from the body of possible RLSs obtained by fitting the data.

On cobalt foil, using Eq. (7) from the carbide model, the CO coverage increases from 0.4 to 0.8 and the hydrogen coverage decreases from 0.5 to 0.1 when the CO partial pressure increases from 3.5 to 45 kPa. The carbon coverage stays almost constant at $\theta_C = 0.1$. Changes in hydrogen partial pressure does not affect the CO coverage ($\theta_{CO} = 0.7$), but the θ_C decreases from 0.2 to 0.1 and θ_H increases from 0.1 to 0.2 as hydrogen partial pressure increases from 13 to 76 kPa. These findings are in agreement with the coadsorption studies of CO and H_2 on cobalt, where CO adsorption was not affected by simultaneous hydrogen adsorption but CO was able to displace hydrogen on the surface (*41*). Fit of Eq. (7) from the enol-complex model gave approximately equal values for the coverages as the carbide model. The post reaction Auger data shown in Fig. 11 indicates carbon deposition during the reaction. Small amounts of carbon, as detected below 550 K, can be explained either as carbon from CO dissociation or as various CH species left on the surface within both models. The higher amounts of carbon deposited above 550 K strongly point to a

A: Carbide theory

Reaction step	Rate if the step on this line is rate limiting
1. $CO + * \leftrightarrow CO*$	$R = \frac{K_0 p_{CO}}{1 + K_H p_{H_2}^{1/2} + \ldots}$
2. $H_2 + 2* \leftrightarrow 2H*$	$R = \frac{K_0 p_{H_2}}{(1 + K_{CO} p_{CO} + \ldots)^2}$
3. $CO* + * \leftrightarrow C* + O*$	$R = \frac{K_0 p_{CO}}{(1 + K_{CO} p_{CO} + K_H p_{H_2}^{1/2} + \ldots)^2}$
4. $C* + H* \leftrightarrow CH* + *$	$R = \frac{K_0 p_{CO}^{1/2} p_{H_2}^{3/4}}{(1 + K_{CO} p_{CO} + K_H p_{H_2}^{1/2} + p_{CO}^{1/2} p_{H_2}^{1/4} + \ldots)^2}$
5. $CH* + H* \leftrightarrow CH_2* + *$	$R = \frac{K_0 p_{CO}^{1/2} p_{H_2}}{(1 + K_{CO} p_{CO} + K_H p_{H_2}^{1/2} + K_C p_{CO}^{1/2} + \ldots)^2}$
6. $CH_2* + H* \leftrightarrow CH_3* + *$	$R = \frac{K_0 p_{CO}^{1/2} p_{H_2}^{5/4}}{(1 + K_{CO} p_{CO} + K_H p_{H_2}^{1/2} + K_C p_{CO}^{1/2} p_{H_2}^{1/4} + \ldots)^2}$
7. $CH_3* + H* \leftrightarrow CH_4 + 2*$	$R = \frac{K_0 p_{CO}^{1/2} p_{H_2}^{3/2}}{(1 + K_{CO} p_{CO} + K_H p_{H_2}^{1/2} + K_C p_{CO}^{1/2} p_{H_2}^{1/2} + \ldots)^2}$
8. $O* + H* \leftrightarrow OH* + *$	
9. $OH* + H* \leftrightarrow H_2O + 2*$	

B: Enol-complex theory

Reaction step	Rate if the step on this line is rate limiting
1. $CO + * \leftrightarrow CO*$	$R = \frac{K_0 p_{CO}}{1 + K_H p_{H_2}^{1/2} + \ldots}$
2. $H_2 + 2* \leftrightarrow 2H*$	$R = \frac{K_0 p_{H_2}}{(1 + K_{CO} p_{CO} + \ldots)^2}$
3. -	-
4. $CO* + 2H* \leftrightarrow CHOH* + 2*$	$R = \frac{K_0 p_{CO} p_{H_2}}{(1 + K_{CO} p_{CO} + K_H p_{H_2}^{1/2} + \ldots)^3}$
5. $CHOH* + * \leftrightarrow CH_2* + O*$	$R = \frac{K_0 p_{CO} p_{H_2}}{(1 + K_{CO} p_{CO} + K_H p_{H_2}^{1/2} + K_C p_{CO} p_{H_2} + \ldots)^2}$
6. $CH_2* + H* \leftrightarrow CH_3* + *$	$R = \frac{K_0 p_{CO}^{1/2} p_{H_2}^{5/4}}{(1 + K_{CO} p_{CO} + K_H p_{H_2}^{1/2} + K_C p_{CO} p_{H_2} + \ldots)^2}$
7. $CH_3* + H* \leftrightarrow CH_4 + 2*$	$R = \frac{K_0 p_{CO}^{1/2} p_{H_2}^{3/2}}{(1 + K_{CO} p_{CO} + K_H p_{H_2}^{1/2} + K_C p_{CO} p_{H_2} + \ldots)^2}$
8. $O* + H* \leftrightarrow OH* + *$	
9. $OH* + H* \leftrightarrow H_2O + 2*$	

FIG. 13. Proposed reaction mechanisms and equations for reaction rate as functions of CO and H_2 partial pressure if different steps are assumed to be rate limiting. Asterisk (*) denotes a vacant adsorption site and X* a molecule adsorbed on a site. (A) is the model involving CO dissociation and (B) is the enol-complex model.

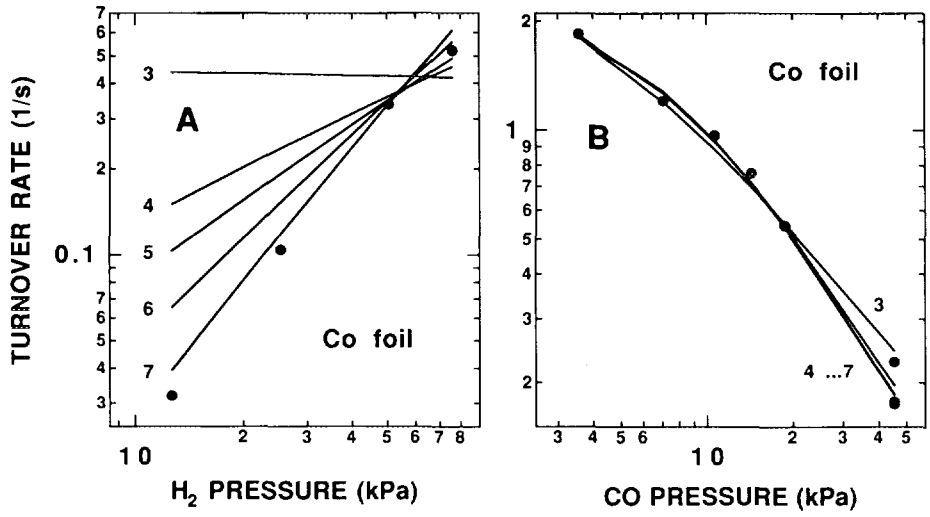

FIG. 14. Measured partial pressure dependence of hydrogen (A) and CO (B) and the model calculations of the partial pressure dependence assuming different elementary reaction steps as rate-determining. The numbers refer to different lines (rate-limiting steps) in the reaction equations.

reaction mechanism involving CO dissociation in accordance with the findings of Geerlings *et al.* (*3*). From all this evidence we concluded that the rate-limiting step on cobalt foil catalyst is the CH_3 hydrogenation within the carbide model.

When the results of the fit obtained using the carbide model to Co/Au data were used to calculate the coverages as functions of partial pressures, hydrogen coverage was found to be more than 99% in all three cases (Eqs. (5), (6), and (7)). This result, which is in contradiction with the CO and H_2 coadsorption data (*41*), lead us to exclude the carbide model in the case of Co/Au. Within the enol-complex model of Fig. 13B, Eqs. (6) and (7) also gave hydrogen coverages close to one. Equations (4) and (5) from the enol-complex model corresponding to CHOH and CH_2 formation, however, gave reasonable values for the surface coverages as functions of the partial pressures exhibiting values ranging between 0.04 and 0.16 for θ_H and between 0.03 and 0.25 for θ_{CO} in case of CHOH formation, between 0.01 and 0.03 for θ_H, and between 0.02 and 0.20 for θ_{CO} in case of CH_2 formation. In both cases the fraction of empty sites on the surface was greater than 0.6. All this evidence lead us to conclude that on the Co/Au system the rate-limiting step is either CHOH or CH_2 formation within the enol-complex model of Fig. 13B.

ACKNOWLEDGMENTS

This work was supported by the Director, Office of Energy Research, Office of Basic Energy Sciences, Material Science Division, U.S. Department of Energy. One of us (J.L.) acknowledges the financial support of Neste Foundation.

REFERENCES

1. Anderson, R. B., "The Fischer–Tropsch Synthesis." Academic Press, New York, 1984.
2. Bartholomew, C. H., *Catal. Lett.* **7**, 303 (1990).
3. Geerlings, J. J. C., Zonnevylle, M. C., and de Groot, C. P. M., *Surf. Sci.* **241**, 302 (1991).
4. Geerlings, J. J. C., Zonnevylle, M. C., and de Groot, C. P. M., *Surf. Sci.* **241**, 315 (1991).
5. Johnson, B. G., Bartholomew, C. H., and Goodman, D. W., *J. Catal.* **128**, 231 (1991).
6. Vannice, M. A., *J. Catal.* **37**, 449 (1975).
7. Fu, L., and Bartholomew, C. H., *J. Catal.* **92**, 376 (1985).
8. Garfunkel, E. L., Parmeter, J., Naasz, B. M., and Somorjai, G. A., *Langmuir* **2**, 105 (1986).
9. Cabrera, A. L., Spencer, N. D., Kozak, E., Da-

vies, P. W., and Somorjai, G. A., *Rev. Sci. Instrum.* **53,** 1888 (1982).
10. Hansen, M., and Anredko, K. "Constitution of Binary Alloys." McGraw–Hill, New York, 1958.
11. Crank, J. "The Mathematics of Diffusion." Clarendon, Oxford, 1976.
12. "Handbook of Auger Electron Spectroscopy," 2nd ed. Physical Electronics Industries, Inc., 1976.
13. Boeglin, C., Carriere, B., Deville, J. P., Heckmann, O., Leroux, C., and Parissod, P., *Surf. Sci.* **211/212,** 767 (1989).
14. Fusy, J., Alnot, M., Abouelaziz, H., and Ehrhardt, J. J., *Surf. Sci.* **251/252,** 573 (1991).
15. Pescia, D., Zampieri, G., Stampanoni, M., Bona, G. L., Willis, R. F., and Meier, F., *Phys. Rev. Lett.* **58,** 933 (1987).
16. Clarke, A., Jennings, G., Willis, R. F., Rous, P. J., and Pendry, J. B., *Surf. Sci.* **187,** 327 (1987).
17. Tikhov, M., and Bauer, E., *Surf. Sci.* **232,** 73 (1990).
18. Zajac, G., Bader, S. D., and Friddle, R. J., *Phys. Rev.* **B 31,** 4947 (1985).
19. Swartz, W. E., Jr., Linn, J. H., Ammons, J. M., and Kovac, M. G., *Thin Solid Films* **114,** 349 (1984).
20. Fogel'son, R. L., Kazimirov, N. N., and Soshnikova, I. V., *Fiz. Met. Metalloved.* **43,** 1105 (1977).
21. Agrawal, P. K., Katzer, J. R., and Manoque, W. H., *Ind. Eng. Chem.* **21,** 385 (1982).
22. Lee, W. H., and Bartholomew, C. H., *J. Catal.* **120,** 256 (1989).
23. Lahtinen, J., Vaari, J., Talo, A., Vehanen, A., and Hautojärvi, P., *Vacuum* **41,** 112 (1990).
24. Je, Y.-T., and Companion, A. L., *Surf. Sci.* **271,** L345 (1992).
25. Dwyer, D. J., and Somorjai, G. A., *J. Catal.* **56,** 249 (1979).
26. Dwyer, D. J., and Somorjai, G. A., *J. Catal.* **52,** 291 (1978).
27. Krebs, H. J., Bonzel, H. P., and Gafner G., *Surf. Sci.* **88,** 269 (1979).
28. Goodman D. W., Kelley, R. D. Madey, T. E., and Yates, J. T., Jr., *J. Catal.* **63,** 226 (1980).
29. Kelley, R. D., and Goodman, D. W., *Surf. Sci.* **123,** L743 (1982).
30. Palmer, R. L., and Vroom, D. A., *J. Catal.* **50,** 244 (1977).
31. Sexton, B. A., and Somorjai G. A., *J. Catal.* **46,** 167 (1977).
32. Castner, D. G., Blackadar, R. L., and Somorjai, G. A., *J. Catal.* **66,** 257 (1980).
33. Rodriguez, J. A., and Goodman, D. W., *Surf. Sci. Rep.* **14,** 1 (1991).
34. Brodén, G., Rhodin, T. N., Brucker, C., Benbow, R., and Hurych, Z., *Surf. Sci.* **59,** 593 (1976).
35. Levin, M. E., Salmeron, M., Bell, A. T., and Somorjai, G. A., *J. Catal.* **106,** 401 (1987).
36. Logan, M., Gellman, A., and Somorjai, G. A., *J. Catal.* **94,** 60 (1985).
37. Bonzel, H. P., and Krebs, H. J., *Surf. Sci.* **117,** 639 (1982).
38. Williams, K. J., Boffa, A. B., Salmeron, M., Bell, A. T., and Somorjai, G. A., *Catal. Lett.* **9,** 415 (1991).
39. Williams, K. J., Ph. D. Thesis, Department of Chemical Engineering, University of California, Berkeley, 1991.
40. Mills, G. A., and Staffgen, F. W., *Catal. Rev.* **8,** 159 (1973).
41. Bridge, M. E., Comrie, C. M., and Lambert, R. M., *J. Catal.* **58,** 28 (1979).